Acta Oceanol. Sin., 2017, Vol. 36, No. 7, P. 110–118
DOI: 10.1007/s13131-017-1087-y
http://www.hyxb.org.cn
E-mail: hyxbe@263.net

The monitoring and analysis of the coastal lowland subsidence in the southern Hangzhou Bay with an advanced time-series InSAR method

HAN Peng[1], YANG Xiaoxia[2, 3]*, BAI Lin[4], SUN Qishi[4]

[1] Administrative Center for China's Agenda 21, Beijing 100038, China

[2] College of Earth Science, Chengdu University of Technology, Chengdu 610059, China

[3] Key Laboratory of Geoscience Spatial Information Technology of Ministry of Land and Resources, Chengdu University of Technology, Chengdu 610059, China

[4] College of Earth Sciences, University of Chinese Academy of Sciences, Beijing 100049, China

Received 17 January 2017; accepted 7 April 2017

Abstract

Time-series InSAR analysis (e.g., permanent scatterers (PSInSAR)) has been proven as an effective technology in monitoring ground deformation over urban areas. However, it is a big challenge to apply this technology in coastal regions due to the lack of man-made targets. An distributed scatterers interferometric synthetic aperture radar (DSInSAR) is developed to solve the problem of insufficient samples and low reliability in monitoring coastal lowland subsidence, by applying a spatially adaptive filter and an eigendecomposition algorithm to estimating the optimal phase of statistically homogeneous distributed scatterers (DSs). Twenty-four scenes of COSMO-SkyMed images acquired between 2013 and 2015 are used to retrieve the land subsidence over the Shangyu District on south coast of the Hangzhou Bay, Zhejiang Province, China. The spatial pattern of the land subsidence obtained by the PS-InSAR and the DSInSAR coincides with each other, but the density of the DSs is three point five times higher than the permanent scatterers (PSs). Validated by precise levelling data over the same period, the DSInSAR method achieves an accuracy of ±5.0 mm/a which is superior to the PS-InSAR with ±5.5 mm/a. The land subsidence in the Shangyu District is mainly distributed in the urban areas, industrial towns and land reclamation zones, with a maximum subsidence rate –30.2 mm/a. The analysis of geological data, field investigation and historical reclamation data indicates that human activities and natural compaction of reclamation material are major causes of the detected land subsidence. The results demonstrate that the DSInSAR method has a great potential in monitoring the coastal lowland subsidence and can be used to further investigate subsidence-related environmental issues in coastal regions.

Key words: coastal areas, land subsidence, DSInSAR, PSInSAR, leveling observation, Hangzhou Bay in China

Citation: Han Peng, Yang Xiaoxia, Bai Lin, Sun Qishi. 2017. The monitoring and analysis of the coastal lowland subsidence in the southern Hangzhou Bay with an advanced time-series InSAR method. Acta Oceanologica Sinica, 36(7): 110–118, doi: 10.1007/s13131-017-1087-y

1 Introduction

More than 100 cities and regions in China have experienced land subsidence, and about 80% are located in coastal areas (Lin et al., 2007). To meet the needs of industrial and agricultural land, beach or land reclamation has been carried out in many coastal areas. The new filled land in reclamation areas is mainly composed of heterogeneous sandy silt and clayey soil and has a short formation time. The weakly consolidated soil is prone to subsidence. In addition, large-scale loading can cause further consolidation of the lower soil layer, leading to large-scale uneven subsidence of reclaimed ground (Törnqvist et al., 2008; Bohannon, 2010; Nicholls and Cazenave, 2010). Coastal terrain is typically low elevations ranging from 2 to 5 m. The annual high water level is similar and the ecological environment is very fragile. In these areas, storm surge, flood, and other natural disasters are frequent (Yuan et al., 2016; Zheng et al., 2002; Fu et al., 2013). Significant land subsidence can lead to disasters such as destruction of urban infrastructure and major engineering deformation instability. Subsidence combined with the global sea level rise can result in ecological and environmental problems like storm surge, reduced flood discharge capacity, damaged port facilities, and saltwater intrusion. These issues exacerbate the deterioration of the coastal environment and lead to economic, environmental and social problems. Therefore, it is important to monitor the land subsidence in coastal areas with high temporal/spatial resolution.

Compared with the conventional land subsidence measurement methods like leveling observation and GPS, differential synthetic aperture radar interferometry (D-InSAR) has the advantages of all-time, all-weather capabilities, large coverage and high spatial/temporal resolution (Hooper et al., 2012), and has been widely used in land subsidence monitoring (Bai et al., 2016; Jiang et al., 2011a). However, it is difficult to carry out high-precision monitoring of long-term slow land subsidence by D-InSAR due to a spatial/temporal decorrelation and an atmospheric disturbance. In order to overcome these limitations, a series of timing series InSAR methods have been proposed. The time series InSAR methods mainly involving a permanent scatterers InSAR

*Corresponding author, E-mail: yangxx2003@126.com

(PSInSAR) method (Ferretti et al., 2001; Hooper et al., 2004), and a small baseline subset (SBAS) method (Berardino et al., 2002; Hooper, 2008), identify and exploit a subset of image pixels which maintain a high coherence level over the study period to acquire a land deformation rate and time series.

The time-series InSAR method has been widely applied in monitoring the coastal land subsidence. The interferometric point target analysis (IPTA) method was used by Jiang and Lin (2010), Jiang et al. (2011a, b) and to monitor land subsidence in reclamation areas of Macau and Hong Kong. The relationship between the land subsidence and the reclamation time was analyzed based on historical reclamation data. Wang et al. (2012) used multitrack SAR data to monitor land subsidence in Shenzhen. The results demonstrate that the average subsidence rate within 500 m of the coast is about –2.5 mm/a. Luo et al. (2014) used TerraSAR-X and PALSAR data to study the land subsidence in the coastal area of Tianjin, and compared subsidence determinants with geological data. Dai et al. (2015) used COSMO-SkyMed and TerraSAR-X data to jointly invert the vertical/horizontal deformation velocity in Shanghai. They find that the vertical deformation rate in Shanghai is in the range of –22.8–9.6 mm/a, and the horizontal velocity in the east-west direction is in the range of –7.2–6.2 mm/a. However, these time series InSAR methods used strict selection of the monitoring point target and required a high coherence level in all of interferograms. Thus, the information of the partially coherent targets and distributed scatterers (DS) in the spatial dimension was discarded (Prati et al., 2010). As a result, the targets with high coherence in the reclamation areas are too sparse to accurately reflect the temporal and spatial variations of the land subsidence, therefore, these methods are limited in coastal land subsidence monitoring.

Taking into account their different statistical behaviors, Ferretti et al. (2011) proposed a new multi-baseline interferometric SAR processing algorithm, referred to as SqueeSAR, to jointly process PS and DS targets. The SqueeSAR has the advantage that joint process can be carried out on the PS and DS targets without causing major changes to the traditional PSInSAR processing flow, and can effectively increase the monitoring target density and improve the monitoring accuracy. However, the SqueeSAR needs to iteratively solve the nonlinear optimal phase. While estimating the initial solution, the SqueeSAR usually needs to insert a damping factor to avoid an invalid eigenvalue which might seriously affect computational efficiency. Goel and Adam (2012) implemented adaptive filtering and coherence estimation according to the DS target, and used the L1 norm for a time series inversion. Taking the underground gas storage in Germany as an example, they used TerraSAR-X data to demonstrate the effectiveness of the method in non-urban areas. Jiang et al. (2016) obtained the surface deformation caused by void fluid extraction and pore pressure reduction in the Lost Hills field in California, USA, using the DSInSAR method based on a fast statistically homogeneous pixel selection. Wang et al. (2016) monitored subsidence in the reclamation areas of Hong Kong using the DSInSAR method. However, the DSInSAR has not been validated and analyzed in the land subsidence monitoring of the coastal areas.

Aiming at the problems mentioned above, a DS point selection method was proposed in this paper, which can greatly improve the computational efficiency by estimating the optimal phase of the DS candidate points using the eigendecomposition algorithm. To verify the effectiveness of this improved DSInSAR method, we selected Shangyu District located on the south bank of Hangzhou Bay as the test cite. Both DSInSAR and PS-InSAR methods were applied to 24 high-resolution COSMO-SkyMed images over Shangyu District from 2013 to 2015 to detect the land subsidence. The InSAR results were evaluated using precise leveling data. Finally, the causes of land subsidence were analyzed using geological data, field surveys, and historical reclamation data.

2 Proposed DSInSAR method

Figure 1 shows the overall framework of the DSInSAR. The basic data processing steps are as follows, first, all the single look complex images (SLC) are registered to the master image, the nonparametric tests is used to select the candidate points of stable DS and the phase of the DS candidate point target is used to perform spatial adaptive filtering and construction of the covariance matrix. Then, the optimal phase is estimated by the eigendecomposition method and substitutes the phase value of the original SAR images. Finally, the selected DS according to the goodness of fit test is processed together with the PS using the

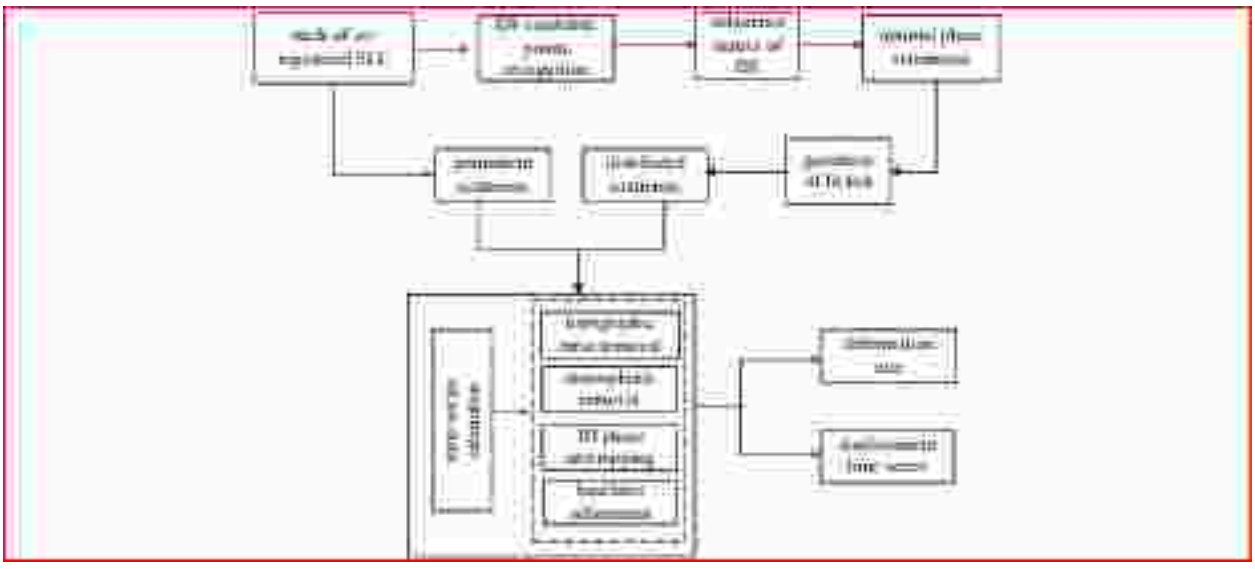

Fig. 1. Framework of DSInSAR data processing.

conventional PSInSAR algorithm for estimating the displacement time series for each measurement point, including terrain error correction, atmospheric error correction, base line refinement and phase unwrapping. The PS point selection and the InSAR time-series analysis method have been discussed previously (Ferretti et al., 2001; Hooper et al., 2007), so here we will not go further on this issue. The following is a brief introduction to the key steps of the DS point selection.

2.1 *DS candidate point recognition*

The DS point target is the coherent accumulation of the echo signals of all the smaller scatterers in the resolution cell, where none of these scatterers have dominant scattering properties (Lee and Pottier, 2009). In radar remote sensing, the radar scattering distribution of the same type of ground objects is similar, and the backscattering characteristics of different ground objects are different. Therefore, the time series of the backscattering can be used as the identification of the DS point. First, the distribution function of the target is defined. If the amplitude time series of two points are consistent with the same probability distribution function, they are considered to have the same backscattering characteristics. The Kolmogorov-Smirnov test (KS test) is usually used to calculate and select the appropriate DS target (Ferretti et al., 2011). The KS test is based on a cumulative distribution function and used to test whether an empirical distribution is consistent with a theoretical distribution or whether there is a significant difference between the two empirical distributions. Suppose that the size of the two samples are n_1 and n_2, and $F_1(X)$ and $F_2(X)$ are respectively used to denote the cumulative empirical distribution functions of the two samples. The approximately normal distribution expression is

$$\begin{aligned} Z &= \max|D_j|\sqrt{\frac{n_1 n_2}{n_1+n_2}}\,, \\ D_j &= F_1(X_j) - F_2(X_j)\,. \end{aligned} \tag{1}$$

The probability distribution function of D can be expressed as

$$P(Z \leqslant x) = 1 - 2\sum_{i=1}^{+\infty}(-1)^{i-1}\mathrm{e}^{-2i^2x^2}. \tag{2}$$

The KS test determines whether the pixel points (X_i) and (X_j) agree with the same distribution by measuring the probability that Z exceeds the threshold x (Stephens, 1970; Seiler and Seiler, 1989).

2.2 *Coherent covariance matrix estimation*

The coherent matrix, which describes the statistics of the distributed scatters target, the interference phase and the coherence coefficient, plays an important role in the same distribution target extraction and parameter estimation (De Zan and Rocca, 2005). As for a pixel point in the SAR image, the mathematic expression of its coherent matrix is

$$\boldsymbol{T} = E[\vec{y}\vec{y}^{\,\mathrm{H}}] \approx \frac{1}{N_P}\sum_{y\in\Omega}\vec{y}\vec{y}^{\,\mathrm{H}}, \tag{3}$$

where $E[\ ]$ is the expectation, $\vec{y} = [y_1, y_2, y_3, \ldots, y_N]$ is the normalized complex observation vector in the time series of the cell; and $E\left[|y_i|^2\right] = 1$.

In practice, the real values of the coherent matrix $\boldsymbol{T}$ is difficult to obtain, so the expected value is often replaced by the average of the pixels in the estimated window. The homogeneous pixels with the same statistical distribution (i.e., DS target) are discriminated from the SAR amplitude images, and they are used for the adaptive spatial filtering based on the DS target to obtain a more accurate interference phase and dryness.

$$\boldsymbol{T} = \begin{bmatrix} 1 & \tilde{\gamma}_{1,2}\mathrm{e}^{j\phi_{1,2}} & \cdots & \tilde{\gamma}_{1,2}\mathrm{e}^{j\phi_{1,N}} \\ \tilde{\gamma}_{1,2}\mathrm{e}^{j\phi_{2,1}} & 1 & \cdots & \tilde{\gamma}_{1,2}\mathrm{e}^{j\phi_{2,N}} \\ \vdots & \vdots & & \vdots \\ \tilde{\gamma}_{1,2}\mathrm{e}^{j\phi_{N,1}} & \tilde{\gamma}_{1,2}\mathrm{e}^{j\phi_{N,2}} & \cdots & 1 \end{bmatrix} = |\boldsymbol{T}| \circ \phi. \tag{4}$$

The absolute values and the phase values of the elements of $\boldsymbol{T}$ are the estimated coherence value $\tilde{\gamma}$ and spatially filtered interferometric phase ϕ, respectively.

2.3 *Estimation of the optimal phase based on eigendecomposition*

The following Eq.(5) can be obtained through decomposing the characteristics of the coherent matrix:

$$\boldsymbol{T} = \sum_{i=1}^{N}\lambda_i\boldsymbol{T}_i = \sum_{i=1}^{N}\lambda_i\vec{U}_i\vec{U}_i^{H}, \tag{5}$$

where λ_i is the eigenvalue, and $\vec{U}_i$ is the eigenvector. Assuming that the effective phase is the first n feature matrices and the latter N-n is the noise phase, and this is

$$\boldsymbol{T} = \sum_{i=1}^{n}\lambda_i\boldsymbol{T}_i + \sum_{i=n+1}^{N}\lambda_i\boldsymbol{T}_i = \boldsymbol{T}_{\mathrm{signal}} + \boldsymbol{T}_{\mathrm{noise}}. \tag{6}$$

In this study, the eigenvalue matrix corresponding to the largest eigenvalue is regarded as a valid signal, therefore, only the first principal component $\vec{U}_1$ is used as the deformation phase. The phase of the eigenvector corresponding to the largest eigenvalue is used as the optimal phase of the DS candidate point (Cao et al., 2016).

2.4 *Goodness of fit*

The goodness of fit is the fitting degree of the entire regression equation. This is used to test the fitting degree of the model to the observed sample value. Assuming that the estimated optimal phase is $\theta = [\theta_1, \theta_2, \ldots, \theta_N]$ and the original interference phase of the nth SLC and the kth SLC is $\phi_{n,k}$, then

$$r = \frac{1}{N^2-n}\sum_{n=1}^{N}\sum_{k\neq n}^{N}\mathrm{e}^{i\phi_{n,k}}\mathrm{e}^{-i(\theta_n-\theta_k)}. \tag{7}$$

The above equation could also be written as

$$r = \frac{2}{N^2-n}\,Re\sum_{n=1}^{N}\sum_{k\neq n}^{N}\mathrm{e}^{i\phi_{n,k}}\mathrm{e}^{-i(\theta_n-\theta_k)}. \tag{8}$$

Equation (7) can be used as an expansion of the time coherence coefficient in the DS. According to the given threshold of r, the DS candidate point that is larger than the threshold is retained and considered as the final DS point.

3 Test site and data set

3.1 *Test site description*

Shangyu District was chosen as the test site, located on the south bank of the Hangzhou Bay, east of Shaoxing City, Zhejiang Province. It covers an area of about 1 400 km^2 (red solid lines in Fig. 2). The topography declines from south to north. The lowland hills in the south and the plain in the north cover 50% of the total land, respectively. The lowland hills in the south belong to two mountain ranges. The hills in the southeast belong to the Siming Mountain which is high and steep; the land hills in southwest belong to the Kuaiji Mountain which has gentle slopes. A water net plain in the north mainly belongs to the Ningshao plain, which has an average elevation of about 5 m; the northernmost tip is the Binhai Gaokang Plain with an average elevation of 10 m. The Ningshao Plain originally derives from marine and lake swamp deposits, with deep soft soil (up to 18–35 m) (Yang, 2003). To meet the demand for agricultural and industrial land, large-scale beach reclamation has been carried out on the south bank of the Qiantang River and Cao'e River Estuaries in Shangyu District since 1969, and the accumulated reclamation area has reached 21 300 hm^2 (Fig. 2) (Liu et al., 2016). A large number of high-rise and super high-rise buildings as well as large-scale infrastructure facilities (Hangzhou–Ningbo high-speed rail, Hangzhou Bay Link High Speed) have been constructed in this area resulting in serious land subsidence in some areas. This subsidence has posed a serious threat to human lives and property and directly affected a sustained development and a social stability.

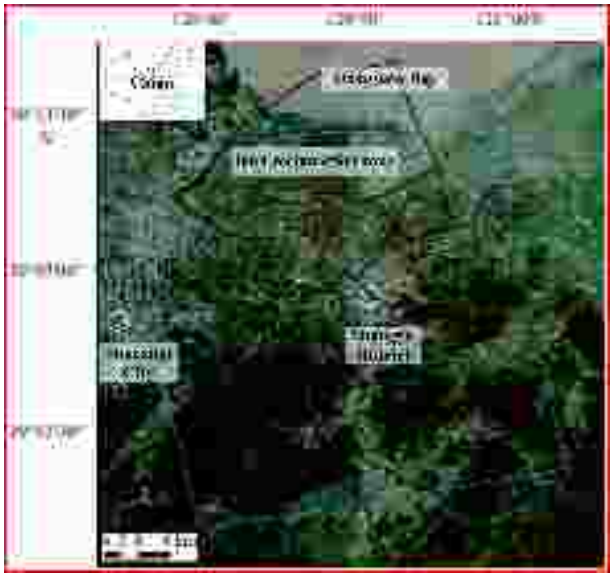

Fig. 2. Location of the study area.

3.2 *Data sets used*

In this study, 24 SAR images with 3 m resolution acquired by COSMO-SkyMed satellites from January 2013 to July 2015 are processed by the PSInSAR and the DSInSAR respectively to obtain land subsidence results in the Shangyu District. The SAR image acquired on August 17, 2014 is selected as the master image. The temporal/perpendicular base line plots of SAR datasets are shown in Fig. 3. The precise leveling data from 2013 to 2015 provided by the First Surveying Mapping Institute of Zhejiang Province are used to evaluate the InSAR-derived results, and the locations of the 37 leveling benchmarks are shown as red triangles in Fig. 2.

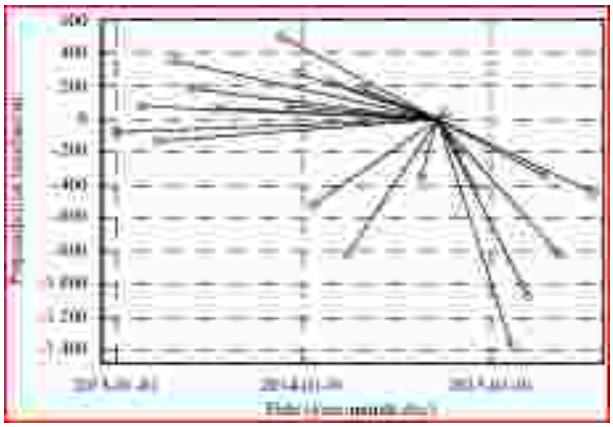

Fig. 3. Temporal/perpendicular baseline plots of SAR data sets.

4 Results and discussion

4.1 *Comparison of results obtained by PSInSAR and DSInSAR*

The land subsidence rates of the Shangyu District from January 2013 to July 2015 acquired by the PSInSAR and the DSInSAR are shown in Fig. 4. The reference point is located at the leveling benchmark named Shangyu National Bedrock Point (white cross). The negative values represent subsidence (green to red) and the positive values represent uplift (light blue to blue). The spatial distributions of the land subsidence obtained by the two methods coincided with each other. The results show rapid land subsidence occurred in some areas and land uplift was ignorable. The subsidence areas were mainly distributed in the northwestern area of Shangyu District (land reclamation zone), the central area (including Shangyu urban zone, Daoxu Town, Songxia Town and Lihai Town) and the southern area (Shangpu Town, Fenghui Town, Dingzhai Town, Xiaguan Town and the northern part of Zhangzhen Town). Distinct subsidence bowls were detected in the land reclamation zone, the Zhangzhen Industrial Park and Xietang Town with a maximum subsidence rate of -30.2 mm/a. The stable region of Shangyu District was mainly concentrated in the Gaibei Town, Tangpu Town, Xiaoyue Town and surrounding hilly areas of Lianghu Town.

In order to validate the InSAR results obtained in this work, we carried out an intercomparison of the InSAR results derived from the PSInSAR and the DSInSAR. The intercomparison method, used in an InSAR validation project of European Space Agency named as PSIC4 (Raucoules et al., 2009), was applied to quantitatively estimating relative difference between the deformation rates derived from the two methods. We randomly extracted 2 000 points from the DS/PS datasets, and then calculated the correlation coefficient. Figure 5 illustrates a scatter-plot of two groups of the averaged deformation rates derived by the DSInSAR and the PSInSAR. The high correlation coefficient (0.798) between them indicates that these two results are consistent with each other.

Using the DSInSAR method, 3 226 377 DS points (≈2 700 km^{-2}) were captured in this study. area, while only 956 428 PS points (≈790 km^{-2}) were captured by the conventional PSInSAR method. The monitoring point density of the former was about three point five times as much as that of the latter. Figure 4 shows that the increasing monitoring points were mainly concentrated in non-urban areas, such as the bare soil and asphalt pavements

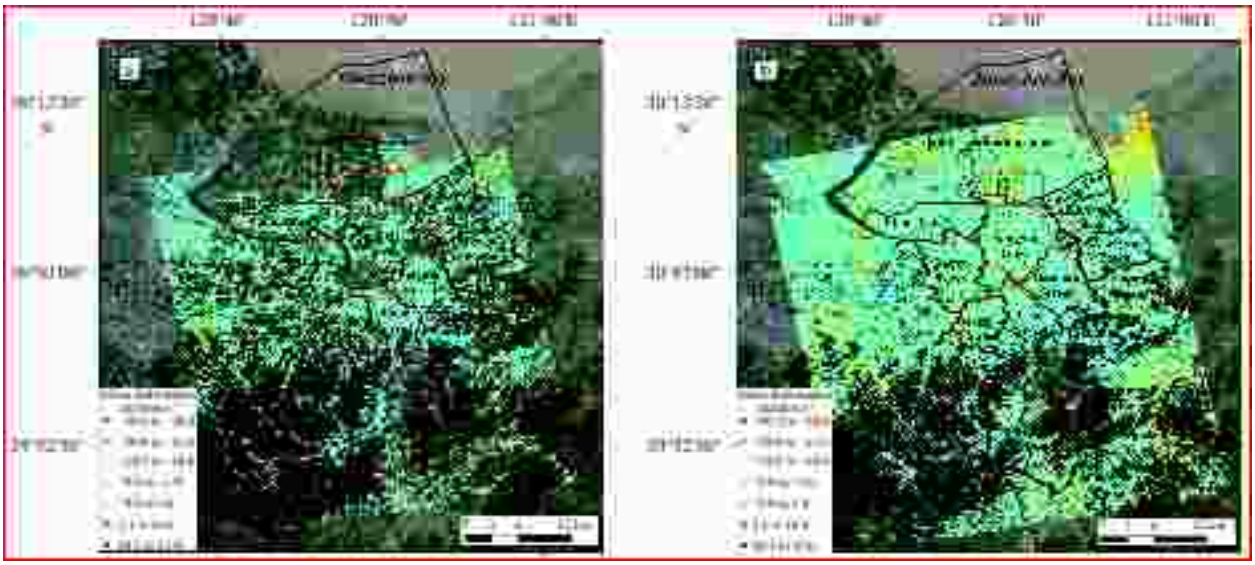

Fig. 4. Subsidence rates of Shangyu District acquired by PSInSAR (a) and DSInSAR (b).

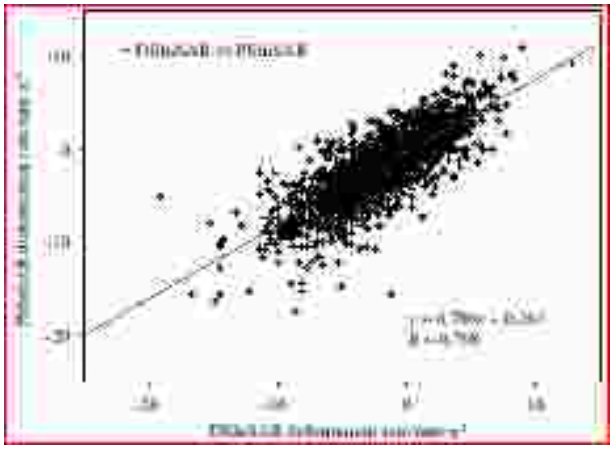

Fig. 5. The correlation between the deformation rates derived by the DSInSAR and the PSInSAR.

with the characteristics of distributed scatterers. Especially in the recent reclamation area of the Hangzhou Bay, Shangyu Industrial Zone, the DS density was six point nine times of the PS density (Table 1). Figure 6 is a zoomed deformation rate map of the vicinity of the east second section in Shangyu Industrial Zone which was a reclamation bare soil area with little buildings distributed. The PSInSAR method can obtain the subsidence of buildings, but cannot identify sufficient PS points to detect the land subsidence in the bare soil region. Nevertheless, the DSInSAR provided complete coverage of land subsidence information and contributed to obtain the knowledge of the spatial distribution of subsidence and discover new subsidence anomaly zones in the area (such as the abnormal subsidence in the white circle in Fig. 6).

Table 1. Statistical results of DS and PS

Typical sample area	Number of monitoring point		Ratio of DS to PS
	DS	PS	
Urban areas	326 401	145 767	2.2
Villages and towns	2 443 370	744 243	3.2
Reclamation area	456 606	66 411	6.9
Total	3 226 377	956 421	3.5

4.2 *Accuracy assessment*

The accuracy of time series InSAR results were evaluated by using the precise leveling results of 37 leveling benchmarks in the study area. The InSAR-derived results were along the radar line-of-sight (LOS) direction, while the leveling measurements were along the vertical direction, so it was necessary to project the leveling results to the radar line-of-sight direction. We evaluated the accuracy of InSAR processing in two ways.

(1) We compared the level bench mark with the DS (PS) points within its 100 m range. If there was no DS (PS) point in the range, the bench mark would not be used for verification. The schematic diagram is shown in Fig. 7a. (2) We used a simple Kriging algorithm, a form of generalized linear regression that provides an optimal spatial estimator by minimizing the mean-squared-error between the measured data and the estimated data at a given location, to interpolate the InSAR results to obtain the spatial continuous deformation results. The InSAR measurements extracted at the level bench marks were used to compare with the leveling results. Figure 7b shows the verification method. All the leveling measured data in the study area could be used to carry out an accuracy evaluation using this method.

The evaluation criteria includes the mean absolute error and the root mean square error of the mutual error between the leveling results and the InSAR results. The mean absolute θ and the root mean square error δ were computed as follows:

$$\theta = \pm \frac{\sum_{i=1}^{N} |d_1 - d_2|}{N}, \tag{9}$$

$$\delta = \pm \sqrt{\frac{\sum_{i=1}^{N} (d_1 - d_2)^2}{N - 1}}, \tag{10}$$

where d_1 is the leveling measurement result, d_2 is the InSAR monitoring result, and N is the number of leveling points.

The accuracy assessments of the DSInSAR and the PSInSAR are shown in Table 2. The mean absolute error and the root mean square error are, respectively, less than 4.5 and 5.5 mm/a, indic-

Fig. 6. Subsidence rates of Shangyu Hangzhou Bay Industrial Park acquired by DSInSAR (a) and PSInSAR (b).

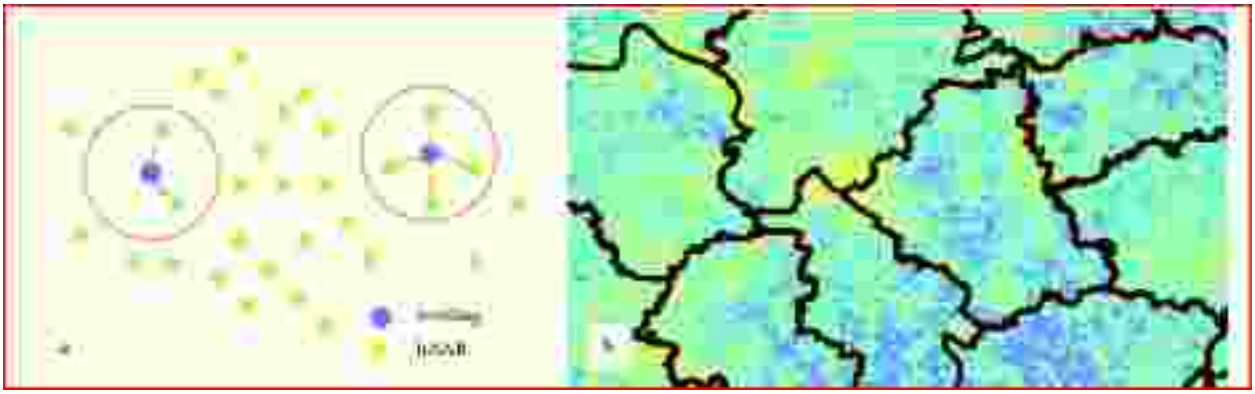

Fig. 7. Diagram of verification using neighboring points (a) and diagram of verification using Kriging interpolation (b).

Table 2. Accuracy assessment of InSAR subsidence monitoring

Method		Mean absolute error/mm·a^{-1}	Root mean square error/mm·a^{-1}
Neighboring points	PS	4.4	5.5
	DS	4.1	5.0
Kriging Interpolation	PS	4.5	5.5
	DS	4.0	4.9

ating that both methods can obtain reliable subsidence rate results. The mean absolute error and root mean square error of the DSInSAR are less than the latter, which indicates that the accuracy of the DSInSAR results is consistent with or even superior to those of the PSInSAR.

4.3 *Causes analysis of land subsidence*

4.3.1 *Urban areas*

The Shangyu urban zone is divided into three parts: Baiguan Road, Cao'e Road and Dongguan Road, and the land subsidence rates are shown in Fig. 8a. The land subsidence was widely distributed in the urban zone, with an average subsidence rate of –2.7 mm/a and a maximum subsidence rate of –23.4 mm/a at the intersection of Xiaoyong Railway and Changtai Expressway (Fig. 8a). Subsidence was mainly distributed in the north of Shangyu, mainly covering the Third Ring Road, the Cao'e River coast which is near to the Songxia Town, along the Xiaoyong railway and the east part of the Dongguan Road. Subsidence was mainly distributed in the new urban area. The major cause of subsidence was the increase of soft ground load and construction drawdown caused by large-scale urban construction. For example, the Binjiang Primary School and its eastern residential area occurred obvious subsidence (Fig. 8a, red rectangle), and the high-rise buildings were under construction on the north side (Fig. 8b blue solid line area). From Fig. 8, we can note that the area adjacent to the construction area was suffering obvious subsidence with a maximum subsidence rate –16 mm/a while there was no significant subsidence signal from the area far from the construction area. Figure 8c shows the structural damage of building caused by the land subsidence in the Binjiang Primary School, indicating that the land subsidence has threatened building safety in this area.

4.3.2 *Villages and towns*

The suburban subsidence areas of Shangyu District were mainly located in the northern plain (Songxia Town, Daoxu Town, Xietang Town, etc.) and the southern hilly valley (Zhangzhen Town, Fenghui Town, Dingzhai Town, etc.). The land subsidence was mainly distributed along roads (such as the Bianli line, the 104 National Road, etc.), and the subsidence centers were all located in large-scale industrial parks (Xietang Town Industrial Park, Zhangzhen Town Industrial Park, etc.). To meet the needs of industrial production, groundwater was overexploited and this was the major cause of regional subsidence here. The extraction of a large amount of water from confined aquifers decreased a water pressure in porous aquifers and increased effective stress, a compression of the aquifer resulted in rapid land subsidence (Chaussard et al., 2014).

The Zhangzhen Industrial Park, which is located on both sides of the 104 National Road, Shangyu City, suffered from the most serious land subsidence. The park region contains industries of metal machinery, textiles, garments, and building decorations. Owing to the large number of high water consumption companies, groundwater overexploitation was serious in the park, and the land subsidence was obvious (Fig. 9). The average

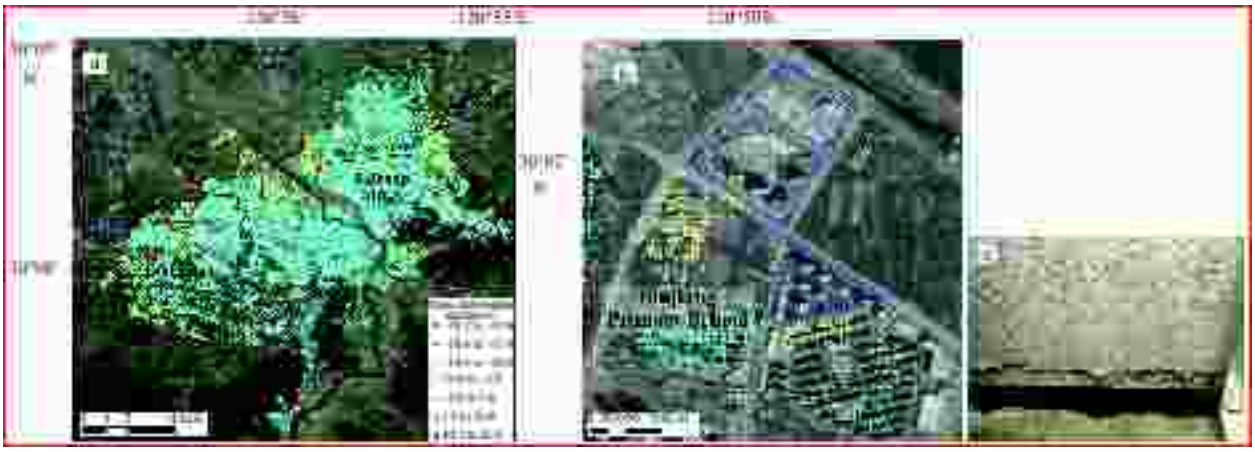

Fig. 8. Average subsidence rates over urban zone (a) and Binjiang Primary School (b), and a photograph of structural damage caused by the land subsidence (c).

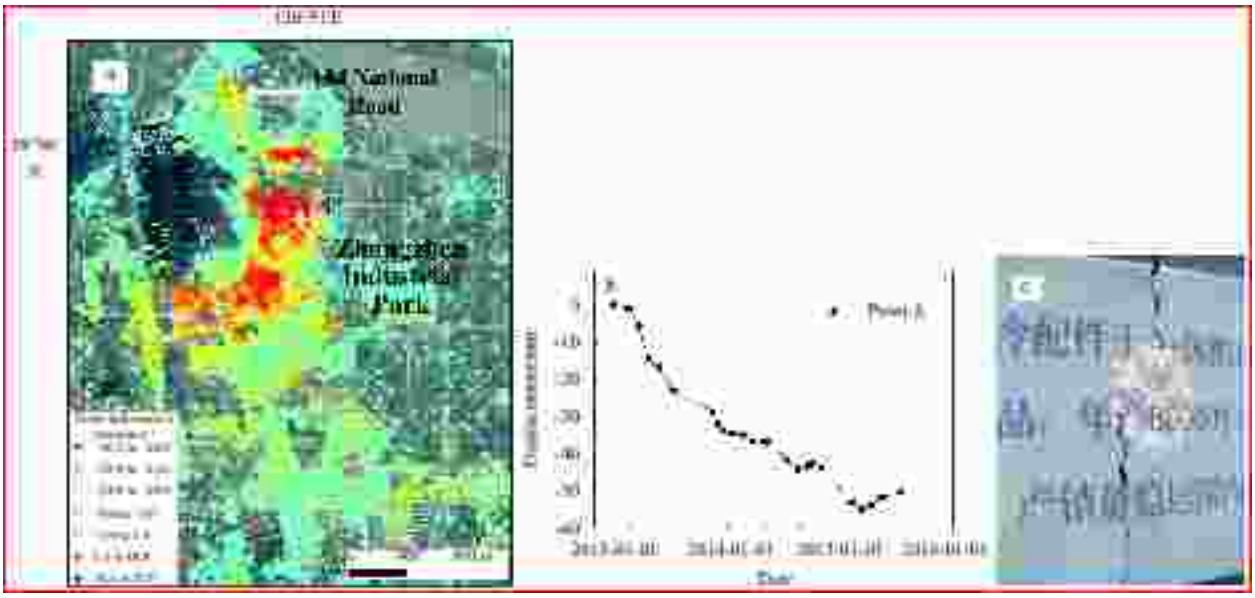

Fig. 9. Average subsidence rate over Zhangzhen Industrial Park (a), displacement time series corresponding to Point A (b), and a photograph of structural damage caused by land subsidence (c).

subsidence rate was –11.4 mm/a and the maximum subsidence rate was –30 mm/a. The maximum cumulative subsidence was nearly 60 mm, which has caused serious building damage (Fig. 9c). Groundwater overuse has also caused a slight subsidence of Changtai Expressway on the west side of the industrial park. The average subsidence rate was –9.9 mm/a and the maximum subsidence rate was –15.2 mm/a.

4.3.3 *Reclamation zone*

Tideland reclamation at Liujiu Hill in the Shangyu District began in 1969. The land reclamation gradually progressed from southwest to northeast, and the cumulative reclamation area has reached 21 300 hm^2 (Liu et al., 2016). The western part of the reclamation zone was mostly used for agriculture and aquaculture while the eastern part was mainly used for the construction of the Hangzhou Bay Shangyu Industrial Park. Figure 10a is the land subsidence rate map in the Shangyu reclamation zone, and the density of the DS points was lower in the western area but higher in the eastern area. The average subsidence rate of the Shangyu reclamation zone was –4.7 mm/a, and the subsidence rate increased from south to north. The maximum subsidence occurred in the northeastern part of the reclamation zone with a subsidence rate of –28.5 mm/a and a cumulative subsidence of more than 50 mm (Fig. 10b). The subsidence of the northeastern part of the reclamation zone was the most serious. Subsidence was associated with the road and the building as the center, and the subsidence rate ranged from –15.0 to –28.5 mm/a. The land subsidence in the western part of the reclamation zone was slightly less than that in the northeast. The subsidence of this area was divided into several independent subsidence centers. The subsidence rate was relatively small, but the subsidence in the northwest was the most serious with a maximum rate of –22 mm/a. Stable areas were mainly distributed in the south of the reclamation zone and areas where lack new roads and construction areas, such as the southeast and southwest parts of the region. The land subsidence in this area was mainly located near the new roads and buildings, and was mainly caused by the compaction of the reclamation materials and the increased load on

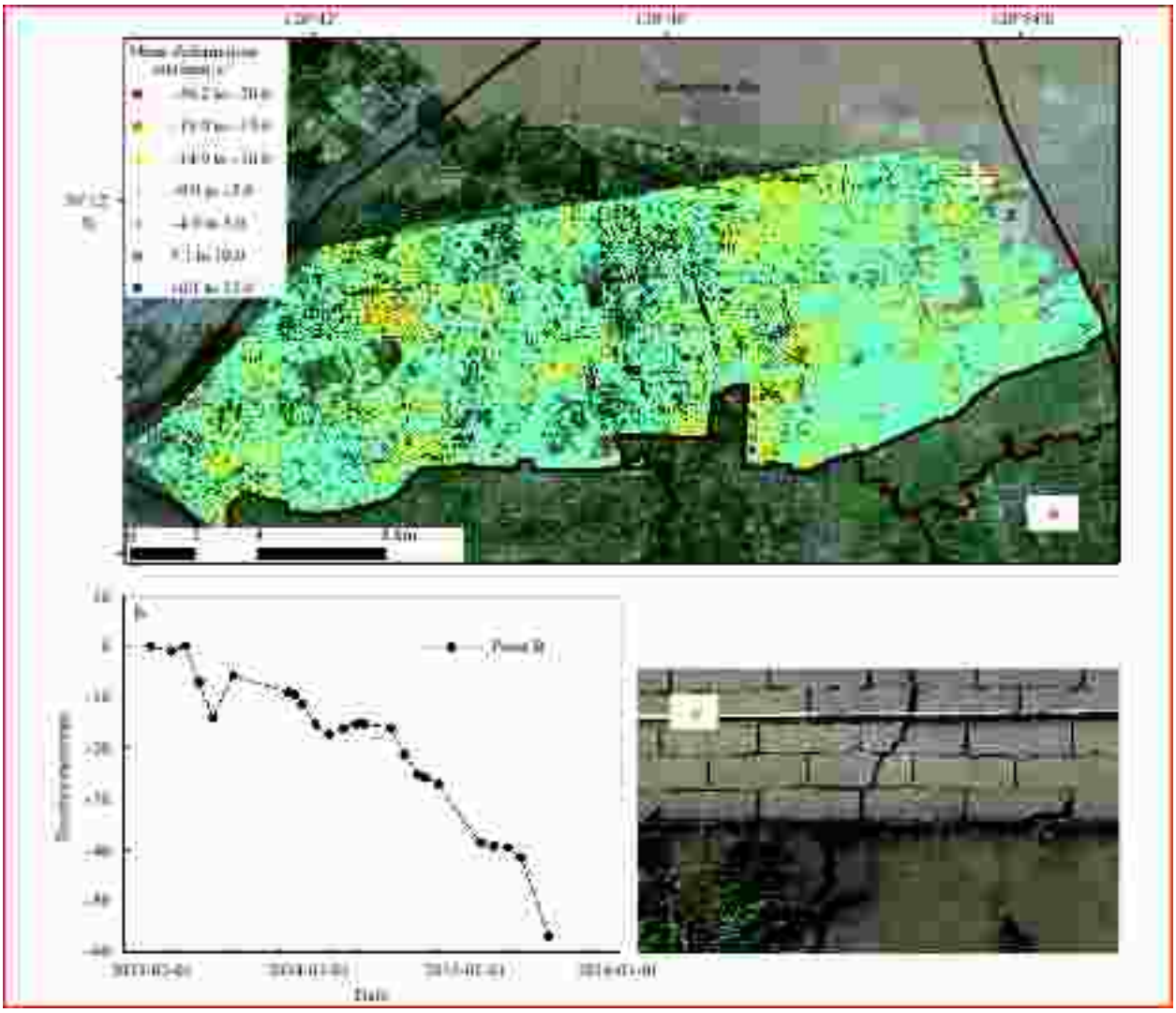

Fig. 10. Average subsidence rate over land reclamation zone (a), displacement time series corresponding to Point B (b), and a photograph of structural damage caused by land subsidence (c).

the soft ground due to the road and building construction.

5 Conclusions

An improved DSInSAR method was developed for a time-series analysis on 24 COSMO-SkyMed images with 3 m resolution to obtain the spatial and temporal evolution of land subsidence fields in the Shangyu District from 2013 to 2015. The accuracy of the InSAR-derived results was evaluated using precise leveling data.

(1) The spatial distributions of land subsidence obtained by the DSInSAR and PSInSAR methods were similar. The density of the DS points was about three point five-fold that of the PS density, and the increased high coherence points were mainly concentrated in non-urban areas, such as bare soil and asphalt pavement, which have the characteristics of distributed scatterers. This indicates that the DSInSAR can obtain high-precision monitoring results in the non-urban areas where artificial targets are absent.

(2) Compared with the leveling measurements, the mean absolute error and root mean square error of the DSInSAR and PSInSAR methods were, respectively, less than ±4.5 mm/a and ±5.5 mm/a. These accuracies demonstrate that both methods can acquire reliable subsidence monitoring results.

(3) Land subsidence in the Shangyu District was mainly distributed in the urban areas, developed towns, and reclamation areas. The maximum subsidence rate reached up to –30.2 mm/a. According to geological data, field surveys, and historical reclamation data, human activities and the natural compaction of reclamation materials were the major causes of the land subsidence.

(4) The DSInSAR method is capable of obtaining high spatial resolution and high precision land subsidence monitoring results in non-urban areas lacking artificial targets. These DSInSAR results could provide a scientific basis and support for the prevention and control of the geological problems related to the land subsidence in the coastal areas.

References

Bai Lin, Jiang Liming, Wang Haisheng, et al. 2016. Spatiotemporal characterization of land subsidence and uplift (2009–2010) over Wuhan in Central China revealed by TerraSAR-X InSAR analysis. Remote Sensing, 8(4): 350

Berardino P, Fornaro G, Lanari R, et al. 2002. A new algorithm for surface deformation monitoring based on small baseline differential SAR interferograms. IEEE Transactions on Geoscience and

Remote Sensing, 40(11): 2375–2383
Bohannon J. 2010. The Nile Delta's sinking future. Science, 327(5972): 1444–1447
Cao Ning, Lee H, Jung H C. 2016. A phase-decomposition-based PSInSAR processing method. IEEE Transactions on Geoscience and Remote Sensing, 54(2): 1074–1090
Chaussard E, Bürgmann R, Shirzaei M, et al. 2014. Predictability of hydraulic head changes and characterization of aquifer-system and fault properties from InSAR-derived ground deformation. Journal of Geophysical Research: Solid Earth, 119(8): 6572–6590
Dai Keren, Liu Guoxiang, Li Zhenhong, et al. 2015. Extracting vertical displacement rates in Shanghai (China) with multi-platform SAR images. Remote Sensing, 7(8): 9542–9562
De Zan F, Rocca F. 2005. Coherent processing of long series of SAR images. In: the IEEE International Geoscience and Remote Sensing Symposium(IGARSS 2005). Seoul, South Korea: Institute of Electrical and Electronics Engineers Inc, 1987–1990
Ferretti A, Fumagalli A, Novali F, et al. 2011. A new algorithm for processing interferometric data-stacks: SqueeSAR. IEEE Transactions on Geoscience and Remote Sensing, 49(9): 3460–3470
Ferretti A, Prati C, Rocca F. 2001. Permanent scatterers in SAR interferometry. IEEE Transactions on Geoscience and Remote Sensing, 39(1): 8–20
Fu Cifu, Yu Fujiang, Wang Peitao, et al. 2013. A study on extratropical storm surge disaster risk assessment at Binhai New Area. Haiyang Xuebao (in Chinese), 35(1): 55–62
Goel K, Adam N. 2012. An advanced algorithm for deformation estimation in non-urban areas. ISPRS Journal of Photogrammetry and Remote Sensing, 73: 100–110
Hooper A. 2008. A multi-temporal InSAR method incorporating both persistent scatterer and small baseline approaches. Geophysical Research Letters, 35(16): L16302
Hooper A, Bekaert D, Spaans K, et al. 2012. Recent advances in SAR interferometry time series analysis for measuring crustal deformation. Tectonophysics, 514–517: 1–13
Hooper A, Segall P, Zebker H. 2007. Persistent scatterer interferometric synthetic aperture radar for crustal deformation analysis, with application to Volcán Alcedo, Galápagos. Journal of Geophysical Research: Solid Earth (1978–2012), 112(B7): B07407
Hooper A, Zebker H, Segall P, et al. 2004. A new method for measuring deformation on volcanoes and other natural terrains using InSAR persistent scatterers. Geophysical Research Letters, 31(23): L23611
Jiang Mi, Ding Xiaoli, He Xiufeng, et al. 2016. FaSHPS-InSAR technique for distributed scatterers: A case study over the lost hills oil field, California. Chinese Journal of Geophysics (in Chinese), 59(10): 3592–3603
Jiang Liming, Lin Hui. 2010. Integrated analysis of SAR interferometric and geological data for investigating long-term reclamation settlement of Chek Lap Kok Airport, Hong Kong. Engineering Geology, 110(3–4): 77–92
Jiang Liming, Lin Hui, Cheng Shilai. 2011a. Monitoring and assessing reclamation settlement in coastal areas with advanced InSAR techniques: Macao city (China) case study. International Journal of Remote Sensing, 32(13): 3565–3588
Jiang Liming, Lin Hui, Ma Jianwei, et al. 2011b. Potential of small-baseline SAR interferometry for monitoring land subsidence related to underground coal fires: Wuda (northern China) case study. Remote Sensing of Environment, 115(2): 257–268
Lee J S, Pottier E. 2009. Polarimetric Radar Imaging: From Basics to Applications. Boca Raton, FL: CRC Press, 53–60
Lin Hui, Jiang Liming, Zhao Qing. 2007. City ground subsidence and monitoring using D-InSAR. Seminar on Disaster Risk Management and Application of Spatial Information Technology in Disaster Prevention and Mitigation (in Chinese). Beijing: China Association for Disaster Prevention
Liu Zhiwei, Zhou Huina, Yu Jia. 2016. Evolution analysis of land development and utilization in Zhejiang Beach Recla mation area based on remote sensing technology: taking Shangyu in Zhejiang Province for example. Zhejiang Hydrotechnics (in Chinese), (2): 49–52, 67
Luo Qingli, Perissin D, Zhang Yuanzhi, et al. 2014. L-and X-band multi-temporal InSAR analysis of Tianjin subsidence. Remote Sensing, 6(9): 7933–7951
Nicholls R J, Cazenave A. 2010. Sea-level rise and its impact on coastal zones. Science, 328(5985): 1517–1520
Prati F, Regar E, Mintz G S, et al. 2010. Expert review document on methodology, terminology, and clinical applications of optical coherence tomography: physical principles, methodology of image acquisition, and clinical application for assessment of coronary arteries and atherosclerosis. European Heart Journal, 31(4): 401–415
Raucoules D, Bourgine B, De Michele M, et al. 2009. Validation and intercomparison of persistent scatterers interferometry: PSIC4 project results. Journal of Applied Geophysics, 68(3): 335–347
Seiler M C, Seiler F A. 1989. Numerical recipes in C: the art of scientific computing. Risk Analysis, 9(3): 415–416
Stephens M A. 1970. Use of the Kolmogorov-Smirnov, Cramér-Von Mises and related statistics without extensive tables. Journal of the Royal Statistical Society: Series B. Methodological, 32: 115–122
Törnqvist T E, Wallace D J, Storms J E A, et al. 2008. Mississippi Delta subsidence primarily caused by compaction of Holocene strata. Nature Geoscience, 1(3): 173–176
Wang Mingzhou, Li Tao, Jiang Liming, et al. 2016. An improvedment coherent targets technology for monitoring surface deformation. Acta Geodaetica et Cartographica Sinica (in Chinese), 45(1): 36–43
Wang H, Wright T J, Yu Y P, et al. 2012. InSAR reveals coastal subsidence in the Pearl River Delta, China. Geophysical Journal International, 191(3): 1119–1128
Yang Lijun. 2003. Engineering geological features and ground treatment in the urban of Shaoxing city (in Chinese) [dissertation]. Hangzhou: Zhejiang University
Yuan Shun, Zhao Xin, Li Linlin. 2016. Combination evaluation and case analysis of vulnerability of storm surge in coastal provinces of China. Haiyang Xuebao (in Chinese), 38(2): 16–24
Zheng Xianxin, Wu Qiang, Ying Yufei, et al. 2002. Problems on land subsidence in China's coastal areas in the 21st century and their solutions. Science & Technology Review (in Chinese), (9): 47–50